

An endoreversible quantum heat engine driven by atomic collisions

Quentin Bouton,^{1,*} Jens Nettersheim,^{1,*} Sabrina Burgardt,¹ Daniel Adam,¹ Eric Lutz,² and Artur Widera^{1,†}

¹*Department of Physics and Research Center OPTIMAS, Technische Universität Kaiserslautern, Germany*

²*Institute for Theoretical Physics I, University of Stuttgart, D-70550 Stuttgart, Germany*

(Dated: September 24, 2020)

Quantum heat engines are subjected to quantum fluctuations related to their discrete energy spectra. Such fluctuations question the reliable operation of quantum engines in the microscopic realm. We here realize an endoreversible quantum Otto cycle in the large quasi-spin states of Cesium impurities immersed in an ultracold Rubidium bath. Endoreversible machines are internally reversible and irreversible losses only occur via thermal contact. We employ quantum control over both machine and bath to suppress internal dissipation and regulate the direction of heat transfer that occurs via inelastic spin-exchange collisions. We additionally use full-counting statistics of individual atoms to monitor heat exchange between engine and bath at the level of single quanta, and evaluate average and variance of the power output. We optimize the performance as well as the stability of the quantum engine, achieving high efficiency, large power output and small power output fluctuations.

Most engines used in modern society are heat engines. Such machines generate motion by converting thermal energy into mechanical work [1]. Two central figures of merit of heat engines are efficiency, defined as the ratio of work output and heat input, and power characterizing the work-output rate. Heat engines should ideally have high efficiency, large power output, and be stable, i.e., exhibit small power fluctuations. However, real thermal machines operate far from reversible conditions and their performance is thus reduced by irreversible losses [2, 3]. At the same time, microscopic motors are exposed to thermal fluctuations and, at low enough temperatures, to additional quantum fluctuations, which are associated with random transitions between discrete levels. Both fluctuation mechanisms contribute to their instability [4, 5]. An important issue is hence to design and optimize small heat engines in order to maximize both their performance and their stability [6].

Nanoscale heat engines have been implemented recently using a single trapped ion [7] and a spin coupled to the single-ion motion [8, 9]. Indications for quantum effects have been reported in a spin engine consisting of nitrogen-vacancy centers interacting with a light field [10], and quantum heat engine operation has been shown in nuclear magnetic resonance [11, 12] and single-ion [9] systems. These thermal machines are based on harmonic oscillators or two-level systems, and the baths mediating heat exchange are simulated by interaction with either laser fields [7–10] or radiofrequency pulses [11, 12].

We here experimentally realize a quantum Otto cycle using a large quasi-spin system in individual Cesium (Cs) atoms immersed in a natural quantum heat bath made of ultracold Rubidium (Rb) atoms. Expansion and compression steps are implemented by varying an external magnetic field, changing the energy-level spacing of the engine and performing work [13]. Heat exchange between system and bath occurs via inelastic endoenergetic and exoenergetic spin-exchange collisions [14]. The increased

number of internal engine states, compared to simple two-level systems, allows for high energy turnover per cycle, while their finite number naturally limits power fluctuations due to saturation, in contrast to the unbound spectrum of harmonic oscillators. We employ quantum control of both the engine’s quasi-spin state and the bath’s spin polarization to control the direction of heat transfer between the two at the level of individual quanta of heat [14], independent of the kinetic thermal state of the bath. This quantum control effectively suppresses internal irreversible losses at the level of individual collisions and thus make the quantum heat engine endoreversible. Endoreversible machines operate internally without any dissipation, while irreversible losses only occur via the contact with the bath. They outperform fully irreversible engines and have played a central role in finite-time thermodynamics for forty years [2, 3]. We additionally characterize the discrete quantum heat transfer at the level of individual quanta using full-counting statistics [15, 16] and monitor the population dynamics of the engine from single-atom and time-resolved measurements of the engine’s quasi-spin distribution along the cycle. We employ this new system and novel techniques to evaluate and optimize the performance as well as the stability of the endoreversible quantum heat engine, achieving high efficiency, large power output and small power output fluctuations.

We experimentally immerse up to ten laser-cooled Cs atoms in the $|F_{\text{Cs}} = 3, m_{F,\text{Cs}} = 3\rangle$ state into an ultracold Rb gas of up to 10^4 atoms in the state $|F_{\text{Rb}} = 1, m_{F,\text{Rb}} = -1\rangle$, both species confined in a common optical dipole trap (Fig. 1(a)) (Appendix A). Here F and m_F denote the total atomic angular momentum and its projection onto the quantization axis, respectively. The quantization axis is given by an external magnetic field of $B_1 = 346.5 \pm 0.2$ mG or $B_2 = 31.6 \pm 0.1$ mG. The Cs atoms quickly thermalize to the kinetic temperature of $T = 950 \pm 50$ nK of the gas. We operate

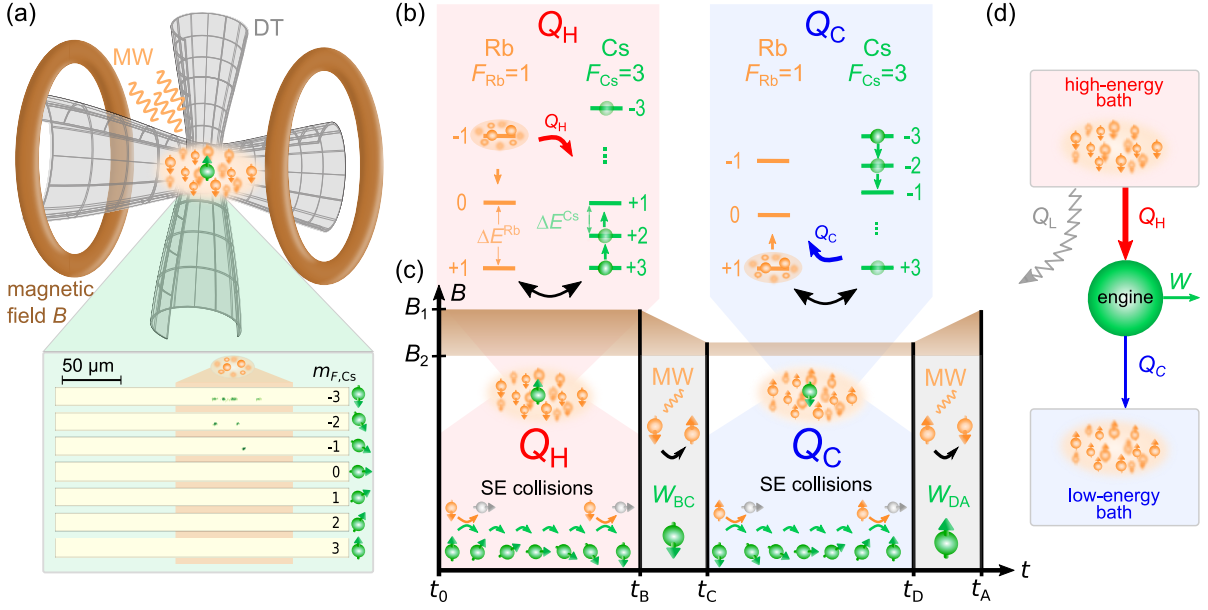


FIG. 1. **Operation principle of the endoreversible quantum heat engine.** (a) Individual laser-cooled Cs atoms (green) are immersed in an ultracold Rb cloud (orange); both are confined in a common optical dipole trap (DT). External magnetic fields and microwave (MW) radiation respectively implement the power strokes of the quantum heat engine and distinguish the high- from the low-energy bath. The inset shows typical m_F -resolved fluorescence images of single Cs atoms for $t = t_B = 300$ ms after initialization. The position of the bath cloud is indicated in orange with a width of 4σ . (b) The heat exchange between the Cs atom (engine) and a Rb (bath) atom occurs via inelastic spin-exchange collisions. Spin polarization of the Rb atoms and spin-conservation in individual collisions allow only up to six exo- or endothermal processes, corresponding to heating or cooling. (c) The experimental Otto cycle consists of a heating stage, during which heat Q_H is absorbed, and a power stroke induced by an adiabatic change of the magnetic field. A microwave field then switches the bath from high to low energy. The cycle is further completed by a cooling step, during which heat Q_C is released, and an additional power stroke when the magnetic field is adiabatically brought back to its initial value. (d) Due to the difference of atomic Landé factors between Cs and Rb, the quantum heat engine (green) absorbs heat Q_H and releases heat Q_C (to produce work W), while the bath releases more energy. The lost energy is irreversibly dissipated during an average of ten elastic collisions and is described by a heat leak Q_L from the high-energy bath.

the quantum heat engine in the spin-state manifold of the seven Cs hyperfine ground states $|F_{Cs} = 3, m_{F,Cs}\rangle$, $m_{F,Cs} \in \{+3, +2, \dots, -3\}$. The states are energetically equally spaced with Zeeman energy $E_n^{Cs} = n\lambda B$, with $\lambda = |g_F^{Cs}|\mu_B$, where $g_F^{Cs} = -1/4$ is the Cs Landé factor, μ_B Bohr's magneton and $n = 3 - m_{F,Cs}$ [18], with the zero-point of energy set to the lowest-energy state $|m_{F,Cs} = 3\rangle$.

Heat between the quantum engine and the bath is exchanged at the microscopic level via inelastic spin-exchange collisions (Fig. 1(b)). Each collision changes the value of the quasi-spin of the Cs engine by $\Delta m_{Cs} = \mp 1\hbar$ leading to an energy change of $\Delta E^{Cs} = \pm \lambda B$ for each Cs atom, and $\Delta m_{Rb} = \pm 1\hbar$ for one Rb atom corresponding to the energy change $\Delta E^{Rb} = \mp \kappa B$, with $\kappa = |g_F^{Rb}|\mu_B$, where $g_F^{Rb} = -1/2$ is the Rb Landé factor [14]. The spin population thus directly reflects the energy exchange between engine and reservoir at the level of single energy quanta. The direction of the heat transfer is determined by the spin polarization of the Rb bath and by angular momentum conservation during individual collisions. The spin polarization of the Rb atoms distin-

guishes a high-energy bath for $m_{Rb} = -1$ from a low-energy bath for $m_{Rb} = +1$. Control over the internal Rb state accordingly permits to either increase or decrease the energy of the quasi-spin of the engine. Heat exchange automatically stops after six spin-exchange collisions, because then the highest/lowest energy state has been reached. The collision transfers the colliding Rb atom to the $|F_{Rb} = 1, m_{F,Rb} = 0\rangle$ state, which forms the exhaust of the engine. Due to the massive imbalance between the Rb and Cs atom numbers ($N_{Rb}/N_{Cs} > 1000$), each collision occurs with a bath atom in the initial state with high probability, making the bath Markovian.

The quantum Otto cycle consists of four parts: one compression and one expansion step, during which work is performed, and a heating and a cooling stage, during which heat is exchanged [13]. The corresponding experimental sequence is shown in Fig. 1(c). The Cs machine is first driven by up to six spin-exchange collisions into energetically higher states (at magnetic field B_1), absorbing heat Q_H in time $\tau_H = t_B$. Work W_{BC} is then performed by adiabatically decreasing the magnetic field to B_2 in $\tau = t_C - t_B = 10$ ms. This time is much longer

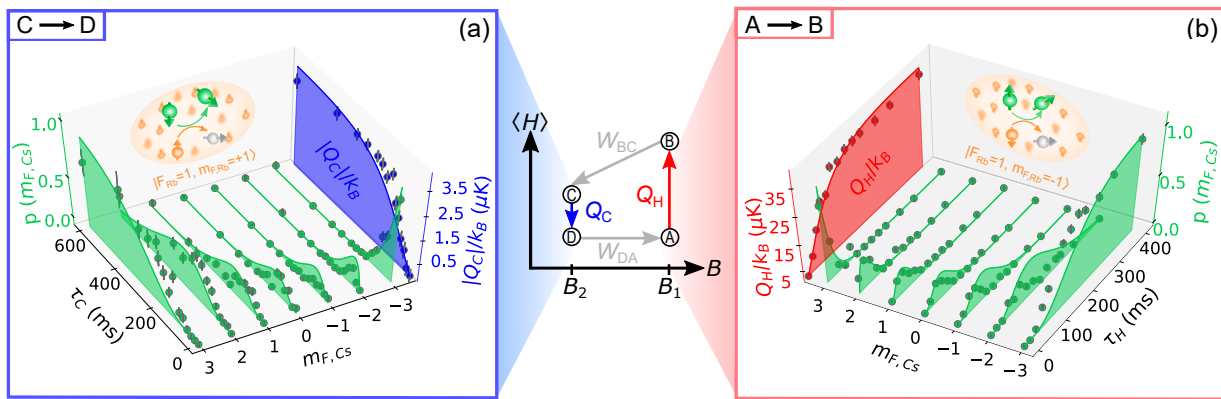


FIG. 2. **Full-counting statistics of heat exchange.** During the heating (AB) and cooling (CD) steps of the quantum Otto cycle (center), heat is exchanged with the bath. The population dynamics of the individual engine levels are shown in green. The averages of heat, Q_H and Q_C , extracted from the full counting statistics are indicated for (a) cooling (blue) and (b) heating (red), as a function of the respective times τ_H and τ_C . Dots show the experimental data, solid lines are a prediction of a microscopic model (Appendix C). In both panels, the population dynamics shows the transition from an initially spin-polarized engine state via a state of many populated m_F levels to a spin polarized state of the other extreme spin state. The inversion of an initially fully polarized population ($|m_{F,Cs} = 3\rangle \leftrightarrow |m_{F,Cs} = -3\rangle$) requires some hundreds of milliseconds.

than the inverse energy splitting ΔE of the quasi-spin states, making the process adiabatic. It is, however, fast enough to avoid unwanted spin-exchange collisions, implying that no heat is transferred. The engine is subsequently brought into contact with the low-energy bath by flipping the spins of the Rb bath using microwave (MW) sweeps. The Cs engine is accordingly driven by up to six spin-exchange collisions into energetically lower states, releasing heat Q_C in time $\tau_C = t_D - t_C$. Work W_{DA} is further performed by adiabatically increasing the magnetic field back to B_1 in $\tau = t_A - t_D = 10$ ms. The Rb spins are finally flipped to their initial state with other microwave sweeps, restoring the high-energy bath.

While each single collision is coherent and thus amenable to quantum state engineering, coupling of the engine to the large number of bath modes in elastic collisions destroys the coherence between the engine's quasi-spin levels. Heat is thus associated with changes of occupation probabilities, $Q = \sum_n E_n \Delta p_n$, whereas work corresponds to changes of energy levels, $W = \sum_n p_n \Delta E_n$ [13]. In our system, we concretely have $Q_H = \sum_n n (p_n^B - p_n^A) \lambda B_1$ for the heating process and $Q_C = \sum_n n (p_n^D - p_n^C) \lambda B_2$ for the cooling process. On the other hand, the respective work contributions for expansion and compression are given by $W_{BC} = \sum_n n p_n^B \lambda (B_2 - B_1)$ and $W_{DA} = \sum_n n p_n^D \lambda (B_1 - B_2)$. In order to evaluate these quantities, we determine the magnetic fields B_1 and B_2 with the help of Rb microwave spectroscopy (Appendix A). We further detect the Zeeman populations p_n^i of individual Cs atoms at arbitrary times by position resolved fluorescence measurements combined with Zeeman-state selective operations [17]. From a series of such measurements, we can, atom by atom, construct the quasi-spin populations at any time

(Fig. 2). This allows us to monitor for the first time the discrete heat exchange between engine and environment with a resolution of single quanta at each time (Fig. 2): the progressive transfer from low (high) energy states to high (low) energy states during heating (cooling) as a function of time is clearly seen (green dots). From the measured heat counting statistics, we compute average (blue and red dots) and variance of heat exchange (Appendix D). We will use these quantities to examine the power output of the quantum machine and its fluctuations.

We first characterize the performance of the quantum Otto engine by evaluating its efficiency given by [13],

$$\eta = \frac{Q_H - |Q_C|}{Q_H + Q_L}, \quad (1)$$

where $Q_H - |Q_C|$ is the total work produced by the thermal machine, Q_L the energy dissipated during the total heat exchange in one cycle, and $Q_H + Q_L$ the heat emitted by the high-energy bath (Fig. 1(d)). Indeed, due to the different atomic Landé factors for Rb ($g_F^{\text{Rb}} = -1/4$) and Cs ($g_F^{\text{Cs}} = -1/2$), only half ($\gamma = g_F^{\text{Cs}}/g_F^{\text{Rb}} = 1/2$) of the energy change of a bath atom is effectively exchanged with the heat engine during an inelastic spin-exchange collision [17]. As a result, the heat emitted (absorbed) by the bath differs from the energy portions absorbed Q_H (emitted Q_C) by the machine. We macroscopically account for the remaining lost energy, which is irreversibly dissipated during an average of ten elastic collisions, by a heat leak [19] equal to $Q_L = \sum_n n (p_n^B - p_n^A) \kappa (1 - \gamma) (B_1 - B_2)$ with $\gamma = \lambda/\kappa$ the ratio of the Landé factors (Appendix B). We obtain

$$\eta = \frac{\gamma(B_1 - B_2)}{B_1 - B_2 + \gamma B_2} \leq 1 - \frac{B_2}{B_1} = \eta_{\text{max}}. \quad (2)$$

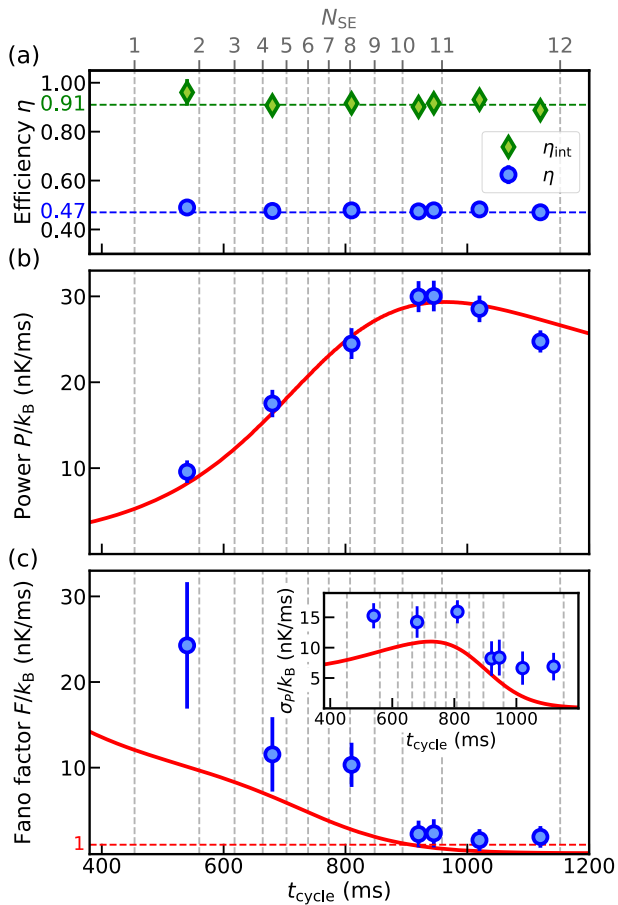


FIG. 3. **Performance of the quantum heat engine.** (a) Efficiency η , Eq. (2) (blue dots), and internal (dissipationless) efficiency η_{int} (green diamonds) for different cycle times; dashed lines indicate the respective expected values. (b) Power output, Eq. (3) (blue dots: experimental data, red solid line: theoretical model), with maximal value reached after almost 12 spin exchange collisions. (c) Fano factor, Eq. (4), and time-resolved fluctuations σ_P (inset). In all cases, the dashed vertical lines (upper axis) indicate the number of spin-exchange collisions N_{SE} . The different durations between two successive spin-exchange collisions originate from different atomic transition rates [14].

Its maximum value η_{max} , reached in the absence of irreversible losses ($\gamma = 1$), is determined by the ratio of the two magnetic fields. We evaluate the efficiency (2) using experimental data for different cycle durations, $\tau_{cycle} = \tau_H + \tau_C + 2\tau$, by varying the heating and cooling times (Fig. 3(a)). We find a constant value, i.e. independent of the number of spin-exchange collisions, of $\eta = 0.478 \pm 0.002$. We emphasize that the internal efficiency of the quantum Otto engine, $\eta_{int} = 1 - |Q_C|/Q_H = 0.917 \pm 0.009$ (Appendix B) is close to the maximal value $\eta_{max} = 0.908$. We may therefore conclude that irreversible losses mainly occur during heat transfer processes, while the engine itself runs reversibly. The quantum heat engine is hence endoreversible. We further note

that, since heat losses are determined by the value of the Landé factors, they can in principle be reduced by choosing different atomic species.

Second, we consider the average power of the quantum heat engine which reads

$$P = \frac{Q_H - |Q_C|}{\tau_{cycle}} \leq \frac{Q_H}{\tau_{cycle}} \left(1 - \frac{B_2}{B_1}\right). \quad (3)$$

We use the heat counting statistics to track its time evolution in Fig. 3(b). We observe that the power (blue dots) increases with the number of inelastic collisions and reaches a maximum, $P_{max}/k_B = 30$ nK/ms, for a cycle time of 960 ms. The corresponding number of inelastic collisions responsible for the heat exchange is almost twelve collisions total (6 spin-exchange collisions for the heating process and 6 for the cooling). This maximum nearly coincides with full population inversion between these two processes ($|m_{F,Cs} = 3\rangle \leftrightarrow |m_{F,Cs} = -3\rangle$), in analogy to a laser. Good agreement with a theoretical model (red solid line) is observed (Appendix C). From a collisional perspective, the energy transfer with the atomic bath is optimal in the sense that it exchanges the maximum energy of six quanta, which can be stored in the machine, in exactly six spin-exchange collisions as a consequence of quantum engineering of the machine's and bath's spin states. The value of P_{max} may be further optimized by enhancing the magnetic field difference, as well as the collision rate and the collision cross-section by controlling the temperature or density of the Rb gas.

We finally investigate the stability of the quantum Otto engine by analyzing the relative power fluctuations via the Fano factor, which quantifies the deviation from a Poisson distribution [20],

$$F_P = \frac{\sigma_P^2}{P} = \frac{\langle P^2 \rangle - \langle P \rangle^2}{P}, \quad (4)$$

where σ_P^2 is the variance of the power, which we determine from the measured quasi-spin distributions (Appendix D). Figure 3(c) displays the Fano factor as a function of the cycle time, with the absolute fluctuations σ_P shown in the inset. We find super-Poissonian fluctuations ($F_P > 1$) for short cycle times, indicating that the quantum engine is unstable in this regime, with large relative power fluctuations. However, with increasing cycle time, the power increases faster than its variance, leading to a decrease in relative fluctuations. The transition to a Poissonian statistics ($F_P = 1$) (red dashed line), with strongly reduced power fluctuations and significantly increased stability, is located approximately at maximum power. This behavior follows from the finite Hilbert space of the Cs machine and the saturation effect due to the existence of an upper energy level. Importantly, the latter effect causes even the absolute value of the power fluctuations to decrease after on average six collisions (Fig. 3(c) inset). Power fluctuations could, in principle, also be

come sub-Poissonian ($F_P < 1$), but this regime is not seen experimentally due to experimental imperfections.

In conclusion, we have realized an endoreversible quantum Otto cycle using single Cs atoms interacting with a Rb bath. The key asset of this machine is the quantum control over both the few-level engine and the atomic reservoir. This unique feature allows us not only to regulate and monitor the heat exchange between system and environment at the single-quantum level, but also to operate the quantum engine in a regime of high efficiency, large power output and small power output fluctuations. The produced work could in principle be extracted by coupling to the magnetic moment of the Cs atoms in a changing external magnetic field. Our system provides a versatile experimental platform to elucidate fundamental new effects generated by quantum reservoir engineering, such as nonequilibrium atomic baths [21, 22] and squeezed baths [23, 24], as well non-Markovian heat reservoirs by reducing the size of the Rb cloud [25, 26].

We thank E. Tiemann for providing us with the scattering cross-sections underlying our numerical model, and T. Busch and J. Anglin for helpful comments on the manuscript. This work was funded by Deutsche Forschungsgemeinschaft via Sonderforschungsbereich (SFB) SFB/TRR185 (Project No. 277625399) and Forschergruppe FOR 2724.

* J.N. and Q.B. contributed equally to this work.

† email: widera@physik.uni-kl.de

- [1] Y. A. Cengel and M. A. Boles, *Thermodynamics. An Engineering Approach*, (McGraw-Hill, New York, 2001).
- [2] B. Andresen, P. Salamon, and R. S. Berry, *Thermodynamics in finite time*, *Phys. Today* **37**, 62 (1984).
- [3] B. Andresen, *Current trends in finite-time thermodynamics*, *Angew. Chem. Int. Ed.* **50**, 2690 (2011).
- [4] P. Pietzonka and U. Seifert, *Universal Trade-Off between Power, Efficiency and Constancy in Steady-State Heat Engines*, *Phys. Rev. Lett.* **120**, 190602 (2018).
- [5] V. Holubec and A. Ryabov, *Cycling Tames Power Fluctuations near Optimum Efficiency*, *Phys. Rev. Lett.* **121**, 120601 (2018).
- [6] T. Denzler and E. Lutz, *Power fluctuations in a finite-time quantum Carnot engine*, arXiv:2007.01034.
- [7] J. Rosznagel, S. T. Dawkins, K. N. Tolazzi, O. Abah, E. Lutz, F. Schmidt-Kaler, and K. Singer, *A single-atom heat engine*, *Science* **352**, 325 (2016).
- [8] D. von Lindenfels, O. Grab, C. T. Schmiegelow, V. Kaushal, J. Schulz, M. T. Mitchison, J. Goold, F. Schmidt-Kaler and U. G. Poschinger, *Spin Heat Engine Coupled to a Harmonic-Oscillator Flywheel*, *Phys. Rev. Lett.* **123**, 080602 (2019).
- [9] N. Van Horne, D. Yum, T. Dutta, P. Hänggi, J. Gong, D. Poletti and M. Mukherjee, *Single-atom energy-conversion device with a quantum load*, *npj Quantum Information* **6**, 37 (2020).
- [10] J. Klatzow, J. Becker, P. Ledingham, C. Weinzetl, K. Kaczmarek, D. Saunders, J. Nunn, I. Walmsley, R. Uzdin, E. Poem, *Experimental Demonstration of Quantum Effects in the Operation of Microscopic Heat Engines*, *Phys. Rev. Lett.* **122**, 110601 (2019).
- [11] R. J. de Assis, T. M. de Mendonca, C. J. Villas-Boas, A. M. de Souza, R. S. Sarthour, I. S. Oliveira and N. G. de Almeida, *Efficiency of a Quantum Otto Heat Engine Operating Under a Reservoir at Effective Negative Temperatures*, *Phys. Rev. Lett.* **122**, 240602 (2019).
- [12] J. P. S. Peterson, T. B. Batalhao, M. Herrera, A. M. Souza, R. S. Sarthour, I. S. Oliveira and R. M. Serra, *Experimental Characterization of a Spin Quantum Heat Engine*, *Phys. Rev. Lett.* **123**, 240601 (2019).
- [13] R. Kosloff and Y. Rezek, *The Quantum Harmonic Otto Cycle*, *Entropy* **19**, 136 (2017).
- [14] F. Schmidt, D. Mayer, Q. Bouton, D. Adam, T. Lausch, J. Nettersheim, E. Tiemann and A. Widera, *Tailored single-atom collisions at ultra-low energies*, *Phys. Rev. Lett.* **122**, 013401 (2019).
- [15] M. Esposito, U. Harbola and S. Mukamel, *Nonequilibrium fluctuations, fluctuation theorems, and counting statistics in quantum systems*, *Rev. Mod. Phys.* **81**, 1665 (2009).
- [16] H. M. Friedman, B. K. Agarwalla and D. Segal, *Quantum energy exchange and refrigeration: a full-counting statistics approach*, *New J. Phys.* **20**, 083026 (2018).
- [17] Q. Bouton, J. Nettersheim, D. Adam, F. Schmidt, D. Mayer, T. Lausch, E. Tiemann and A. Widera, *Single-atom quantum probes for ultracold gases boosted by nonequilibrium spin dynamics*, *Phys. Rev. X* **10**, 011018 (2020).
- [18] C. Cohen-Tannoudji and D. Guery-Odelin, *Advances in Atomic Physics*, (World Scientific, Singapore, 2011).
- [19] R. Masser and K. H. Hoffmann, *Dissipative Endoreversible Engine with Given Efficiency*, *Entropy* **21**, 1117 (2019).
- [20] U. Fano, *Ionization Yield of Radiations. II. The Fluctuations of the Number of Ions*, *Phys. Rev.* **72**, 26 (1947).
- [21] O. Abah and E. Lutz, *Efficiency of heat engines coupled to nonequilibrium reservoirs*, *EPL* **106**, 20001 (2014).
- [22] R. Alicki, D. Gelbwaser-Klimovsky, *Non-equilibrium quantum heat machines*, *New J. Phys.* **17** 115012 (2015).
- [23] J. Rosznagel, O. Abah, F. Schmidt-Kaler, K. Singer, and E. Lutz, *Nanoscale heat engine beyond the Carnot limit* *Phys. Rev. Lett.* **112**, 03602 (2014).
- [24] J. Klaers, S. Faelt, A. Imamoglu and E. Togan, *Squeezed Thermal Reservoirs as a Resource for a Nanomechanical Engine beyond the Carnot Limit*, *Phys. Rev. X* **7**, 031044 (2017).
- [25] G. Thomas, N. Siddharth, S. Banerjee, and S. Ghosh, *Thermodynamics of non-Markovian reservoirs and heat engines*, *Phys. Rev. E* **97** 062108 (2018).
- [26] M. Pezzutto, M. Paternostro, and Yasser Omar, *An out-of-equilibrium non-Markovian Quantum Heat Engine*, *Quantum Sci. Technol.* **4**, 025002 (2019).
- [27] A. J. Kerman, V. Vuletić, C. Chin, and S. Chu, *Beyond Optical Molasses: 3D Raman Sideband Cooling of Atomic Cesium to High Phase-Space Density*, *Phys. Rev. Lett.* **84** 439 (2000).
- [28] F. Schmidt, D. Mayer, M. Hohmann, T. Lausch, F. Kindermann and A. Widera, *Precision measurement of the ^{87}Rb tune-out wavelength in the hyperfine ground state $F = 1$ at 790 nm*, *Phys. Rev. A* **93**, 022507 (2016).
- [29] F. Schmidt, D. Mayer, Q. Bouton, D. Adam, T. Lausch, N. Spethmann and A. Widera, *Quantum Spin Dynam-*

ics of Individual Neutral Impurities Coupled to a Bose-Einstein Condensate, Phys. Rev. Lett. **121**, 1304031 (2018).

- [30] H. Haken and H. C. Wolf, *The Physics of Atoms and Quanta, Introduction to Experiments and Theory* (Springer, Berlin, Heidelberg, 2005).

SUPPLEMENTARY INFORMATION

A: Experimental procedures

We start our experimental sequence by preparing an ultracold Rb gas in the magnetic field insensitive state $|F_{\text{Rb}} = 1, m_{F,\text{Rb}} = 0\rangle$ and, at a distance of $\approx 200 \mu\text{m}$, a small sample of laser cooled Cs atoms. The Cs atoms are further cooled and optically pumped into the $|F_{\text{Cs}} = 3, m_{F,\text{Cs}} = 3\rangle$ hyperfine ground state by employing degenerate Raman sideband-cooling [27]. A species-selective optical lattice [28] transports the Cs atoms into the Rb cloud. MW radiation prepares the bath atoms in the state $|F_{\text{Rb}} = 1, m_{F,\text{Rb}} = -1\rangle$. The starting point of the heat engine cycle is defined by switching off the optical lattice potential. After a predefined time t_i , the Cs-Rb interaction is stopped by freezing the positions of the Cs atoms using the optical lattice, and pushing the Rb cloud out of the trap with a resonant laser pulse. State-selective fluorescence imaging of the Cs atoms completes the procedure [29].

The high-energy and low-energy baths are interchanged by transferring the Rb atoms from $|F_{\text{Rb}} = 1, m_{F,\text{Rb}} = -1\rangle$ to $|F_{\text{Rb}} = 1, m_{F,\text{Rb}} = +1\rangle$ and vice versa using two successive Landau-Zener sweeps. The transfer takes ~ 4.4 ms, which is fast enough to avoid spin-exchange interactions during the state change of the bath.

The two magnetic fields B_1 and B_2 defining the quantization axis for the engine operation, are measured using Rb microwave spectroscopy on the $|F_{\text{Rb}} = 1, m_{F,\text{Rb}} = 0\rangle \rightarrow |F_{\text{Rb}} = 2, m_{F,\text{Rb}} = +1\rangle$ transition. The population of the Rb atoms in state $|F_{\text{Rb}} = 2, m_{F,\text{Rb}} = +1\rangle$ is detected by standard absorption imaging, using a time-of-flight measurement (Fig. 4). We fit the measured data with a standard model to extract the transition frequency, which translates into a magnetic field value using the Breit-Rabi formula [30]. We find typical errors of the order of 0.1 mG.

The magnetic field changes extracting work of the engine have to be adiabatic, i.e., preserving the populations p_n . The adiabaticity condition writes $\omega_{\text{lar}}/\omega_{\text{lar}}^2 \ll 1$, where $\omega_{\text{lar}} = |g_F^{\text{Rb}}|\mu_B B/\hbar$ is the Larmor frequency. It can therefore be expressed as

$$A \equiv \frac{\hbar \dot{B}}{|g_F|\mu_B B^2} \ll 1. \quad (5)$$

Experimentally, we linearly vary the magnetic field from $B_1 = 346.5 \pm 0.2$ mG to $B_2 = 31.6 \pm 0.1$ mG in a time scale of 10 ms, yielding values of $A(B_1) = 0.2 \times 10^{-3}$ and $A(B_2) = 14 \times 10^{-3}$, thus fulfilling the adiabatic condition at any time during the variation of the magnetic field. Moreover, the time scale of the magnetic field variation is faster than the time scale associated to the spin exchange collisions (see number of collisions over time in

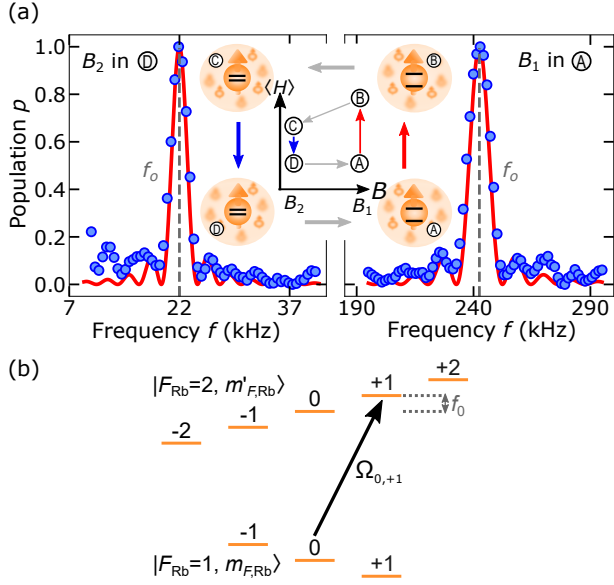


FIG. 4. **Magnetic field extraction.** Rb microwave spectra for extraction of the magnetic fields B_1 and B_2 (a) and corresponding transition scheme (b). Center of (a) illustrates the engine cycle and the corresponding Zeeman energy splitting of a Rb bath atom. Red lines correspond to the theory curves and blue dots are experimental data. These measurements yielding magnetic fields $B_1 = 346.5 \pm 0.2$ mG and $B_2 = 31.6 \pm 0.1$ mG. Measured spectra confirm similar magnetic fields for B and C.

Fig. 3). Hence, the populations p_n are constant during the isentropic processes ($B \rightarrow C$ and $D \rightarrow A$).

B: Efficiency of the endoreversible machine

We calculate the efficiency by distinguishing two different forms of heat exchange. First, we consider the respective energies given (Q_1) and taken (Q_2) by the baths, where $Q_1 - |Q_2|$ is the energy turnover of the reservoirs per cycle. Second, we consider the energies absorbed (Q_H) and rejected (Q_C) from the engine, where $Q_H - |Q_C|$ is the energy turnover of the machine. Both quantities differ because of the different atomic Landé factors of Cs and Rb. The difference $Q_L = (Q_1 - |Q_2|) - (Q_H - |Q_C|)$ is dissipated via elastic collisions and irreversibly lost. We macroscopically model it as a heat leak from the high-energy reservoir. Using the population distribution of the quasi-spin levels at the cycle points in Fig. , the

individual heats can be calculated, leading to

$$Q_L = (Q_1 - |Q_2|) - (Q_H - |Q_C|) \\ = \left(\sum_n n [p_n^B - p_n^A] \kappa B_1 - \left| \sum_n n [p_n^D - p_n^C] \kappa B_2 \right| \right) \\ - \left(\sum_n n [p_n^B - p_n^A] \lambda B_1 - \left| \sum_n n [p_n^D - p_n^C] \lambda B_2 \right| \right). \quad (6)$$

Due to preservation of populations during adiabatic strokes, we can further use $p_n^D = p_n^A$ and $p_n^B = p_n^C$, yielding the expression for the dissipated heat

$$Q_L = \sum_n n (p_n^B - p_n^A) (\kappa - \lambda) (B_1 - B_2). \quad (7)$$

The efficiency is calculated as the work, $|W| = Q_H - |Q_C|$, produced by the engine, divided by the energy provided by the high-energy bath, $Q_H + Q_L$. Using $p_n^D = p_n^A$, $p_n^B = p_n^C$ and $\gamma = \lambda/\kappa$, we find

$$\eta = \frac{Q_H - |Q_C|}{Q_H + Q_L} = \frac{\gamma(B_1 - B_2)}{B_1 - B_2 + \gamma B_2}. \quad (8)$$

The internal efficiency of the engine is computed as the ratio of the produced work $|W|$ and the heat absorbed by the machine Q_H :

$$\eta_{\text{int}} = \frac{Q_H - |Q_C|}{Q_H} = 1 - \frac{B_2}{B_1}. \quad (9)$$

It corresponds to the efficiency without a leak ($\gamma = 1$).

C: Microscopic model and number of collisions

The quantum heat exchange between engine and bath is based on the understanding of individual spin-exchange collisions. In general, the spin-collision rate $\Gamma^{m_F \rightarrow m_F \pm 1}$ is different both for every initial state m_F and for the direction, i.e., $\Delta m_F = \pm 1$. The individual rates are well known from coupled-channel calculations of the molecular interaction potential between Rb and Cs [14]. These rates allow us to describe the evolution with a rate model [17] that captures the spin dynamics and yields excellent agreement with the experimental data. From these rates, we also compute the mean number of spin collisions N_{spin} within a cycle duration $t = t_D$ in two steps. First, we calculate the time-averaged collision rate as the sum of time-averaged collision rates during heating (exothermal spin collisions) and cooling (endothermal spin collisions) as

$$\langle \Gamma(t) \rangle = \langle \Gamma_{A \rightarrow B}(t) \rangle + \langle \Gamma_{C \rightarrow D}(t) \rangle \\ = \sum_{m_F=+3}^{-2} p_{m_F}(t) \Gamma_{A \rightarrow B}^{m_F \rightarrow m_F-1} \\ + \sum_{m_F=+2}^{-3} p_{m_F}(t) \Gamma_{C \rightarrow D}^{m_F \rightarrow m_F+1} \quad (10)$$

Second, we integrate these rates during the heating and cooling to obtain the number of collisions within cycle time t as

$$\begin{aligned} N_{\text{spin}}(t) &= N_{\text{A} \rightarrow \text{B}} + N_{\text{C} \rightarrow \text{D}} \\ &= \int_0^{t_{\text{B}}} \langle \Gamma_{\text{A} \rightarrow \text{B}}(t') \rangle dt' + \int_{t_{\text{C}}}^{t_{\text{D}}} \langle \Gamma_{\text{C} \rightarrow \text{D}}(t') \rangle dt'. \end{aligned} \quad (11)$$

In order to close the cycle, the initial and final Cs states before and after a cycle have to be the equal, leading to the condition $N_{\text{A} \rightarrow \text{B}} = N_{\text{C} \rightarrow \text{D}}$.

D: Fluctuations of the quantum machine

To extract the fluctuations of the engine, Eq. (4), we calculate the power, Eq. (3), via $P = |W|/\tau_{\text{cycle}}$. The cycle time $\tau_{\text{cycle}} = t_{\text{D}}$ is experimentally controlled, and we assume that it is a fixed parameter not adding further fluctuations to the power-output fluctuations. Therefore, we can restrict the calculation to the fluctuations σ_W of work W as $\sigma_W^2 = \langle W^2 \rangle - \langle W \rangle^2$. The work is given by the difference of energy absorbed by and rejected from the engine $|W| = Q_{\text{H}} - |Q_{\text{C}}|$, and hence

$$\begin{aligned} \sigma_W^2 &= \sigma_{Q_{\text{H}}}^2 + \sigma_{Q_{\text{C}}}^2 \\ &= \langle Q_{\text{H}}^2 \rangle - \langle Q_{\text{H}} \rangle^2 + \langle Q_{\text{C}}^2 \rangle - \langle Q_{\text{C}} \rangle^2. \end{aligned} \quad (12)$$

The averages and variances of heat absorbed or rejected depend on the energy differences at the different points during the cycle, for example, $Q_{\text{H}} = E(t_{\text{B}}, B_1) - E_0(t_0, B_1)$. Here $E(t_i, B_j) = \sum_n p_n^i(t_i) n \lambda B_j$ can be computed from the measured quantum-level populations $\{p_n^i\}$ of level n at point $i = \text{A, B, C, D}$ during the cycle and the magnetic field B_j ($j = 1, 2$), together with mean energy and variance. Then, the fluctuations σ_Q^2 of heat Q exchanged when changing the engine's probability distribution from point i to point f at a magnetic field B_j reads

$$\begin{aligned} \sigma_Q^2 &= \sum_n (p_n^f(t_f) + p_n^i(t_i)) (n \lambda B_j)^2 \\ &\quad - \left\{ \left[\sum_n p_n^f(t_f) n \lambda B_j \right]^2 + \left[\sum_n p_n^i(t_i) n \lambda B_j \right]^2 \right\}, \end{aligned} \quad (13)$$

where, using the notation of Fig. 1(c), for Q_{H} $i = 0$, $f = \text{B}$, and $B_j = B_1$, and for Q_{C} $i = \text{C}$, $f = \text{D}$, and $B_j = B_2$. Inserting these expressions into Eq. (12) allows us to compute the work fluctuations for every cycle time $\tau_{\text{cycle}} = t_{\text{A}}$ and thereby the variance of the output power fluctuations σ_P^2 .